ELSEVIER

Journal of Wind Engineering
and Industrial Aerodynamics 91 (2003) 219–229

JOURNAL OF wind engineering AND industrial aerodynamics

www.elsevier.com/locate/jweia

Large-eddy simulation of turbulent airflow over complex terrain

Takanori Uchida*, Yuji Ohya

Research Institute for Applied Mechanics, Kyushu University, 6-1 Kasuga-koen, Kasuga-city, Fukuoka 816-8580, Japan

Abstract

In order to develop an overall efficient and accurate method of predicting an unsteady three-dimensional airflow over a complex terrain with characteristic length scales on the order of kilometers, we recently developed the CFD codes referred to as the RIAM-COMPACT (Research Institute for Applied Mechanics, Kyushu University, Computational Prediction of Airflow over Complex Terrain). In this paper, we carried out the calculation of turbulent airflow over a real complex terrain in a horizontal region of 9.5 km × 5 km with a relatively fine spatial resolution of 50 m. This area covers the new campus of Kyushu University. In order to generate instantaneous velocity fluctuations in an approaching flow, an unsteady flow field in the driver unit is directly calculated. The numerical results obtained by RIAM-COMPACT demonstrated that the changes induced on the wind field by the topographic effect, such as the local wind acceleration and the flow separation, were successfully simulated. We emphasized the following features as regards the wind field over the new campus area under the influence of the west wind. The wind field in the central region of the new campus area is strongly influenced by the wake region generated behind Mt. Hiyama (244 m). The airflows moving around the side of Mt. Hiyama exhibit relatively small fluctuations. When these winds reach Mt. Ishigateke (99 m), they are locally accelerated at the peak. Consequently, a local speed-up effect is confirmed in the southern part of the new campus area.

Keywords: Finite-difference method; Local wind system; Complex terrain; Large-eddy simulation; Cartesian non-uniform staggered grid; Generalized curvilinear collocated grid

1. Introduction

Recently, computational fluid dynamics (CFD) has become one of the most useful tools in wind engineering, mainly due to advancements made in computer

*Corresponding author. Fax: +81-92-583-7779.
E-mail address: takanori@riam.kyushu-u.ac.jp (T. Uchida).

0167-6105/02/$ - see front matter
PII: S0167-6105(02)00347-1

performance, i.e., hardware, software, and graphic capabilities. At present, the approach presented here is widely recognized as computational wind engineering (CWE) [1].

We have been developing a couple of CFD codes, which are referred to as the RIAM-COMPACT (Research Institute for Applied Mechanics, Kyushu University, Computational Prediction of Airflow over Complex Terrain) [2,3]. The basic objective of this numerical study was to develop an overall efficient and accurate method of simulating the wind field ranging from the meso scale to the local scale. For example, these CFD codes can play an important role in wind energy exploitation activities. Numerical results can produce three-dimensional wind distributions that cannot be obtained, even by extensive experimental and field measurements. In addition, they can describe the changes induced on the wind field by topographic effects.

The RIAM-COMPACT consists of three-dimensional time-dependent CFD codes, which are based on a direct [2] and large-eddy [3] simulation using a finite-difference method (FDM). A direct numerical simulation (DNS), in which all scales of turbulent motions from the largest scales down to the dissipation scales must be resolved and no turbulence model is introduced, is not practical for CWE applications. A large-eddy simulation (LES) approach is conceptually more suitable for the forecasting of the local wind field over a complex terrain, because the large-scale turbulent motion that is directly affected by the boundary conditions is computed explicitly, whereas only the effect of the small-scale motion that tends to be more isotropic and dissipative has to be modeled. At present, LES calculations are computationally expensive. However, it should be added here that, from the viewpoint of the aforementioned situations, this approach has a notable advantage over the Reynolds-averaged (RANS) turbulence model, and thus the present approach might prove to be a promising method in the near future.

In this paper, the characteristics of the RIAM-COMPACT are briefly described, with an emphasis on the LES technique. Next, these LES codes are applied to the calculation of turbulent airflow over a real complex terrain in a horizontal region of $9.5\,\mathrm{km} \times 5\,\mathrm{km}$ with a relatively fine spatial resolution of 50 m. This area covers the new campus of Kyushu University. In order to generate instantaneous velocity fluctuations in an approaching flow, an unsteady flow field in the driver unit, which is set upstream of the computational domain covering the topography, is directly calculated. Particular emphasis is placed on whether the changes induced on the wind field by the topographic effect, such as the local wind acceleration and the flow separation, can be successfully simulated.

2. The characteristics of the RIAM-COMPACT

2.1. Governing equations

We consider a three-dimensional airflow of incompressible and viscous fluid over a complex terrain with characteristic length scales on the order of kilometers, so that

the Coriolis force can be neglected. In a DNS, the dimensional governing equations consist of the continuity and Navier–Stokes equations, as follows:

$$\frac{\partial u_i}{\partial x_i} = 0, \tag{1}$$

$$\frac{\partial u_i}{\partial t} + u_j \frac{\partial u_i}{\partial x_j} = -\frac{1}{\rho_0}\frac{\partial p}{\partial x_i} + \frac{\mu}{\rho_0}\frac{\partial^2 u_i}{\partial x_j \partial x_j}, \tag{2}$$

where the subscripts i and $j = 1$, 2, and 3 correspond to the streamwise (x), spanwise (y), and vertical (z) directions, respectively. In the above equations, u_i is the instantaneous velocity component in the i-direction, p is the instantaneous pressure, ρ_0 is the reference density, and μ is the viscosity coefficient. All the variables are non-dimensionalized by an appropriate velocity U_{ref} and a length scale h, such as $u_i^* = u_i/U_{\mathrm{ref}}$ and $x_i^* = x_i/h$, resulting in the following dimensionless equations:

$$\frac{\partial u_i}{\partial x_i} = 0, \tag{3}$$

$$\frac{\partial u_i}{\partial t} + u_j \frac{\partial u_i}{\partial x_j} = -\frac{\partial p}{\partial x_i} + \frac{1}{Re}\frac{\partial^2 u_i}{\partial x_j \partial x_j}, \tag{4}$$

where Re ($= \rho_0 U_{\mathrm{ref}} h/\mu$) is the Reynolds number, and the asterisk is omitted.

In an LES, the flow variables are divided into a grid-scale (GS) part and a subgrid-scale (SGS) part by the filtering operation. The filtered continuity and Navier–Stokes equations written in non-dimensional form are given by

$$\frac{\partial \bar{u}_i}{\partial x_i} = 0, \tag{5}$$

$$\frac{\partial \bar{u}_i}{\partial t} + \bar{u}_j \frac{\partial \bar{u}_i}{\partial x_j} = -\frac{\partial \bar{p}}{\partial x_i} - \frac{\partial \tau_{ij}}{\partial x_j} + \frac{1}{Re}\frac{\partial^2 \bar{u}_i}{\partial x_j \partial x_j}, \tag{6}$$

where $\bar{u}_i$ is the instantaneous filtered velocity component in the i-direction, and $\bar{p}$ is the instantaneous filtered pressure. The effect of the unresolved SGSs appears in the SGS stress as follows:

$$\tau_{ij} = \overline{u_i u_j} - \bar{u}_i \bar{u}_j, \tag{7}$$

which must be modeled. In this study, τ_{ij} is parameterized by an eddy viscosity assumption of Smagorinsky [4] through the following constitutive relations:

$$\tau_{ij} - (\delta_{ij}/3)\tau_{kk} = -2\nu_{\mathrm{SGS}}\bar{S}_{ij}, \tag{8}$$

$$\nu_{\mathrm{SGS}} = (C_{\mathrm{s}} f_{\mathrm{s}} \Delta)^2 |\bar{S}|, \tag{9}$$

$$f_{\mathrm{s}} = 1 - \exp(-z^+/25), \tag{10}$$

$$|\bar{S}| = (2\bar{S}_{ij}\bar{S}_{ij})^{1/2}, \tag{11}$$

$$\bar{S}_{ij} = \frac{1}{2}\left(\frac{\partial \bar{u}_i}{\partial x_j} + \frac{\partial \bar{u}_j}{\partial x_i}\right), \tag{12}$$

$$\Delta = (h_x h_y h_z)^{1/3}, \tag{13}$$

where δ_{ij} is the Kronecker delta, v_{SGS} is the eddy viscosity, $\bar{S}_{ij}$ is the resolved strain-rate tensor, C_s is the dimensionless model coefficient (i.e., Smagorinsky constant), which is multiplied by the Van Driest exponential wall damping function f_s in order to account for the near wall effect, Δ is the grid-filter width, which is a characteristic length scale of the largest SGS eddies, and $|\bar{S}|$ is the magnitude of the resolved strain-rate tensor.

2.2. Coordinate system and variable arrangement

The most important factor involved in a successfully accurate simulation of airflow over complex terrain is correctly determining how to specify the topography model as the boundary conditions in the computation. For this purpose, we examine two coordinate systems and their corresponding variable arrangement, as shown in Figs. 1 and 2. The first system involves a Cartesian non-uniform staggered grid, where the Cartesian velocity components are defined at the mid-point on their corresponding cell surfaces, whereas only the pressure is defined at the center of a cell, as shown in Figs. 1(a) and 2(a). The other system is a generalized curvilinear collocated grid, where the Cartesian velocity components and pressure are defined at the center of a cell, while the volume flux components multiplied by the Jacobian are defined at the mid-point on their corresponding cell surfaces, as shown in Figs. 1(b) and 2(b). In the case of a Cartesian non-uniform staggered grid, the rectangular grids represent the topography model imposed in the calculation. If we employ a Cartesian

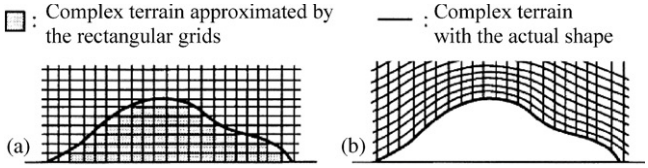

Fig. 1. Coordinate system: (a) cartesian coordinate system; (b) generalized curvilinear coordinate system.

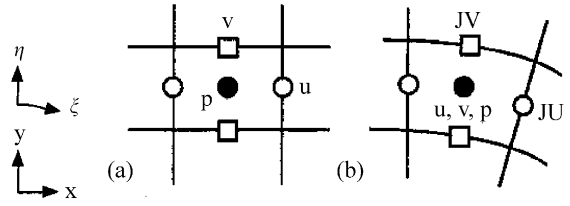

Fig. 2. Variable arrangement: (a) staggered grid; (b) collocated grid.

non-uniform staggered grid, then the original governing equations in the physical space are directly discretized without any coordinate transformation. On the other hand, if we employ a generalized curvilinear collocated grid, then the original governing equations in the physical space are transformed to the computational space through a coordinate transformation. As a result, the discretized governing equations based on a Cartesian non-uniform staggered grid become simpler than those based on a generalized curvilinear collocated grid. However, it should be noted here that both the CFD codes show the same results in terms of CPU time and overall airflow characteristics over a complex terrain [2].

2.3. Numerical method

The coupling algorithm of the velocity and pressure fields is based on a fractional step method [5] with the Euler explicit scheme. Therefore, the velocity and pressure fields are integrated by the following procedure. In the first step, the intermediate velocity field is calculated from the momentum equations without the contribution of the pressure gradient. In the next step, the pressure field is computed iteratively by solving the Poisson equation with the successive over relaxation (SOR) method. Finally, the divergence-free velocity at the $(n+1)$th time step is then obtained by correcting the intermediate velocity field with the computed pressure gradient. As for the spatial discretization in the governing equations, a second-order accurate central difference approximation is used, except for the convective terms. For the convective terms written in non-conservation form, a modified third-order upwind biased scheme [6] is used. The weight of the numerical viscosity term is sufficiently small ($\alpha = 0.5$), compared to the Kawamura–Kuwahara scheme ($\alpha = 3$) [7]. The characteristics of the RIAM-COMPACT are summarized in Table 1.

Table 1
Characteristics of the RIAM-COMPACT

	Code I	Code II
Coordinate system	Cartesian coordinate system	Generalized curvilinear coordinate system
Variable arrangement	Staggered grid	Collocated grid
Discretization method	Finite-difference method (FDM)	
Coupling algorithm	Fractional step method	
Time advancement method	Euler explicit method	
Poisson equation for pressure	Successive over relaxation (SOR) method	
Convective terms	3rd-order upwind biased scheme based on an interpolation method ($\alpha = 0.5$)	
Other spatial derivative terms	2nd-order accurate central difference approximation	
SGS model	Standard Smagorinsky model with the wall damping function	

3. Numerical results

Using RIAM-COMPACT based on the LES technique, we consider the calculation of turbulent airflow over a real complex terrain. In the application of the LES to wind engineering problems, the technique of providing the inflow boundary condition is very important, since the periodic boundary condition cannot be used. In the present study, in order to generate instantaneous velocity fluctuations in an approaching flow, an unsteady flow field in the driver unit, which is set upstream of the computational domain covering the topography, is directly calculated by using a Cartesian non-uniform staggered grid. The obtained turbulent airflow is connected as the inflow boundary conditions at every time step; the airflow over a complex terrain is then calculated by using a generalized curvilinear collocated grid.

Fig. 3 shows the location of the new campus area of Kyushu University. Fig. 4 shows the top view of the computational domain covering the topography, together with the upstream driver unit. The computational domain, including Mt. Hiyama ($h = 244$ m), is an extremely complex region, and is 9.5 km $(40h) \times 5$ km $(20h) \times 1.22$ km $(5h)$. Mt. Hiyama is located to the west of the new campus area. In order to consider the significant details of the topography, we use horizontal uniform grids with Δx and $\Delta y = 50$ m $(0.2h)$, and vertical non-uniform grids with $\Delta z = 0.85$ m $(0.0035h) \sim 61$ m $(0.25h)$. The number of grid points in the $\underline{x}$-, $\underline{y}$-, and $\underline{z}$-directions is $201 \times 101 \times 61$ for the upstream driver unit, and is $196 \times 101 \times 61$ for the computational domain covering the topography. The altitudes of the topography are based on digital data provided by the Japan Map Center. We specify the west wind as the forcing wind. To clarify the topographic effect on the wind field near the ground, the surface roughness, such as a forest canopy, is not considered. The boundary conditions for the velocity field in the computational domain covering the

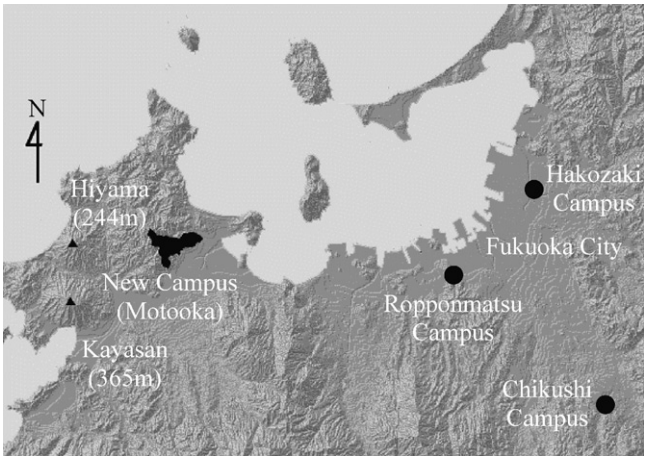

Fig. 3. Location of the new campus area.

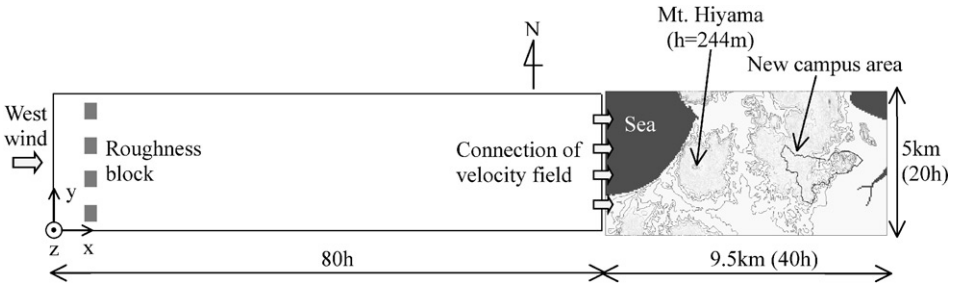

Fig. 4. Top view of the computational domain covering the topography, together with the upstream driver unit.

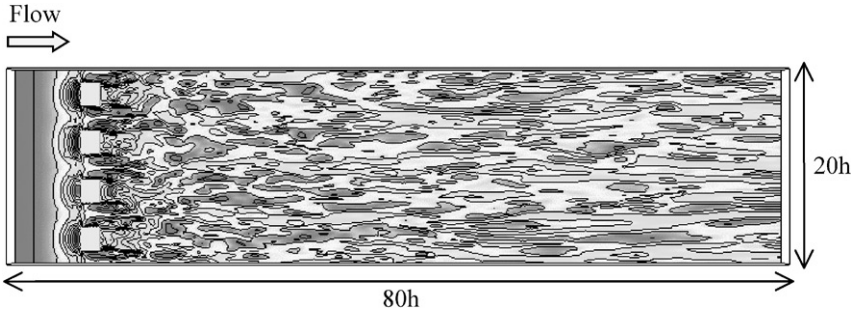

Fig. 5. Top view of instantaneous distributions of the streamwise (x) velocity component ($\bar{u}$) in the upstream driver unit at a height $z^* = 20$ m.

topography are as follows: turbulent airflow connected from the upstream driver unit at every time step (inflow), free-slip condition (top and side boundary), convective outflow condition (outflow) and no-slip condition (ground and topography). The Reynolds number Re ($= \rho_0 U_{\mathrm{ref}} h/\mu$), which is based on the height of Mt. Hiyama ($h = 244$ m) and the mean velocity U_{ref} at the height of Mt. Hiyama in the inflow boundary, is on the order of 10^4. The value of $C_s = 0.1$ is used, and the dimensionless time step Δt is set at 0.001. The computation was carried out on the FUJITSU-VPP5000 computer at the Research Institute for Applied Mechanics (RIAM), Kyushu University. The CPU time of calculation on the VPP5000 was approximately 5 h for about 100 non-dimensional time units.

Fig. 5 shows the top view of instantaneous distributions of the streamwise (x) velocity component ($\bar{u}$) in the upstream driver unit at a height $z^* = 20$ m, i.e., near the ground. The intense velocity fluctuations are generated just downstream of the roughness block, and the formation of low- and high-speed streaks can be clearly observed far away from the roughness block. Fig. 6 shows the rear view of instantaneous streamlines in the upstream driver unit at $x = 76$ h. We can see a number of eddy structures in the vicinity of the ground, which approximately correspond to the coherent structures, such as the streaks and the bursting event.

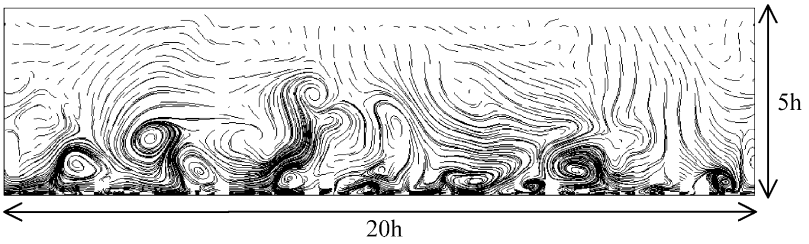

Fig. 6. Rear view of instantaneous streamlines in the upstream driver unit at $x = 76$ h.

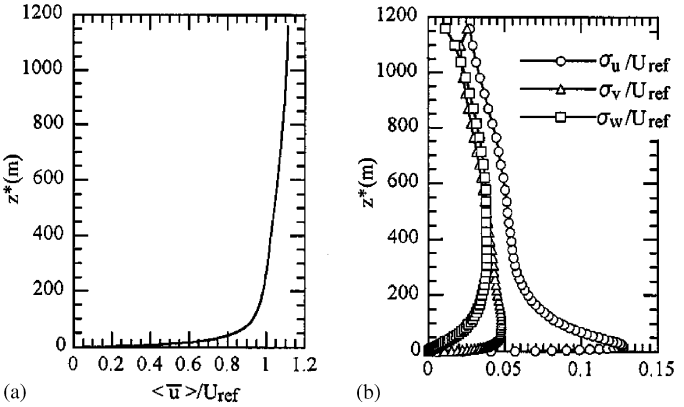

Fig. 7. Turbulence statistics in the upstream driver unit: (a) mean-velocity profile; (b) turbulence intensities in the $\underline{x}$-, $\underline{y}$-, and $\underline{z}$-directions. All the quantities are time- and spanwise-averaged at $x = 76$ h from 200 non-dimensional time units.

Fig. 7(a) shows the mean-velocity profile. Fig. 7(b) shows the vertical profiles of turbulence intensities in the $\underline{x}$-, $\underline{y}$-, and $\underline{z}$-directions. All the quantities are time- and spanwise-averaged at $x = 76$ h from 200 non-dimensional time units. The entrance length behind the roughness block is sufficiently long (72 h), so that the turbulent boundary layer generating on the ground is fully developed.

To visualize the typical airflow patterns over the new campus area under the influence of the west wind, marker particles were successively released at two upstream positions with a non-dimensional time interval of 0.4. Fig. 8 shows the side (Fig. 8(a)) and top (Fig. 8(b)) views of particle movement after 20 intervals. We can see a large difference in fluid motion. The fluctuations of particle motion denoted by A are very large in both the horizontal and vertical directions, because they are strongly influenced by the wake region generated behind Mt. Hiyama (244 m). In contrast, the particle motion denoted by B exhibits relatively small fluctuations, eventually leading to the local wind acceleration near the top of Mt. Ishigateke (99 m), as shown in Fig. 9(a).

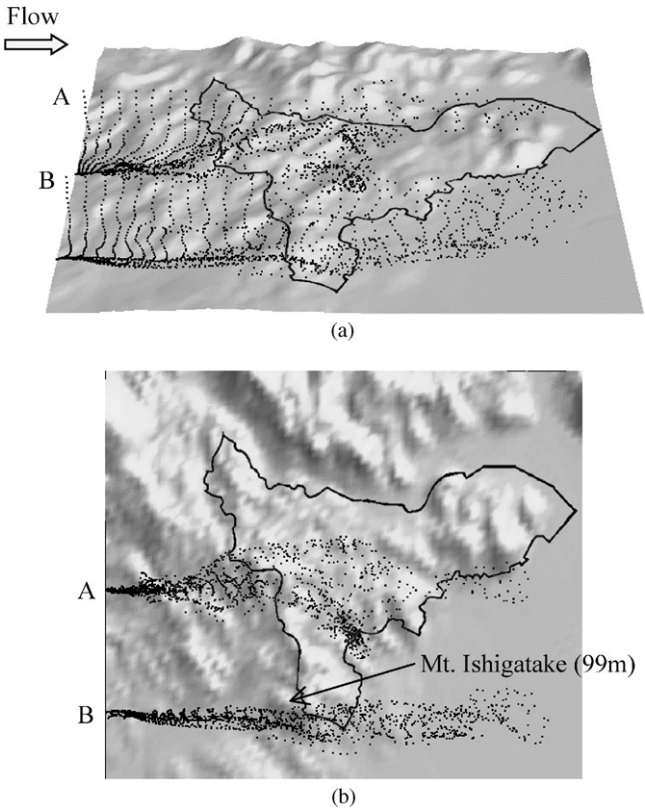

Fig. 8. Particle movement released at two upstream positions of the new campus area: (a) side view; (b) top view. A non-dimensional time interval is $\Delta t = 0.4$, and this figure was obtained after 20 intervals.

Fig. 9 shows the vertical profiles of turbulence statistics at three different locations, i.e., p1, p2, and p3. Fig. 9(a) shows the mean-velocity profile. Fig. 9(b)–(d) shows the turbulence intensities in the $\underline{x}$-, $\underline{y}$-, and $\underline{z}$-directions. All the quantities, which are estimated from 100 non-dimensional time units, are normalized by the ambient velocity U_{ref}, and are shown with the z^* coordinate. At the location of p1, there is a significant velocity defect in the range $100\,\mathrm{m} \leqslant z^* \leqslant 400\,\mathrm{m}$, as shown in Fig. 9(a), due to the wake region generated behind Mt. Hiyama. In addition, the magnitude in the turbulence intensities becomes very large in these ranges, as shown in Fig. 9(b)–(d). On the other hand, at the location of p2, the local wind acceleration is clearly seen near the ground, as shown in Fig. 9(a). It is much more likely that the airflow moving around the side of Mt. Hiyama is locally accelerated at the top of Mt. Ishigateke. Accordingly, the relative magnitude in the turbulence intensities becomes smaller than those obtained at locations p1 and p3 over the whole range, as shown in Fig. 9(b)–(d).

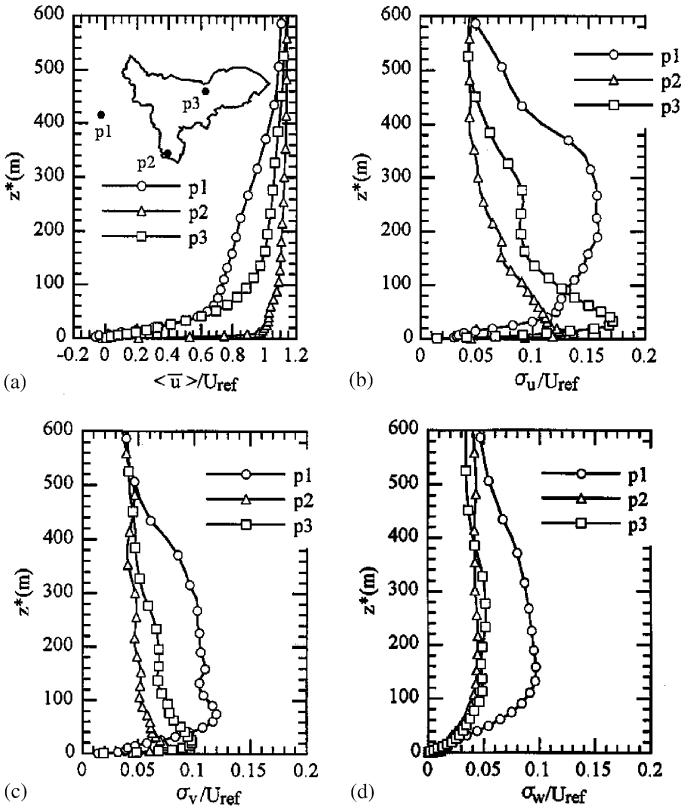

Fig. 9. Turbulence statistics at three different locations, i.e., p1, p2, and p3: (a) mean-velocity profile; (b–d) turbulence intensities in the $\underline{x}$-, $\underline{y}$-, and $\underline{z}$-directions. All the quantities are estimated from 100 non-dimensional time units.

4. Concluding remarks

In order to develop an overall efficient and accurate method of predicting an unsteady three-dimensional airflow over a complex terrain with characteristic length scales on the order of kilometers, we have developed CFD codes referred to as the RIAM-COMPACT. In this paper, we carried out the calculation of turbulent airflow over a real complex terrain covering the new campus area of Kyushu University. In order to generate instantaneous velocity fluctuations in an approaching flow, an unsteady flow field in the driver unit is directly calculated. The numerical results obtained by RIAM-COMPACT demonstrated that the changes induced on the wind field by the topographic effect, such as the local wind acceleration and the flow separation, were successfully simulated. We emphasized the following features as regards the wind field over the new campus area under the influence of the west wind. The wind field in the central region of the new campus area is strongly influenced by the wake region generated behind Mt. Hiyama (244 m). The airflows moving around

the side of Mt. Hiyama exhibit relatively small fluctuations. When these winds reach Mt. Ishigateke (99 m), they are locally accelerated at the peak. Consequently, a local speed-up effect is confirmed in the southern part of the new campus area.

References

[1] S. Murakami, R. Ooka, A. Mochida, S. Yoshida, S. Kim, CFD analysis of wind climate from human scale to urban scale, J. Wind Eng. Ind. Aerodyn. 81 (1999) 57–81.
[2] T. Uchida, Y. Ohya, Numerical simulation of atmospheric flow over complex terrain, J. Wind Eng. Ind. Aerodyn. 81 (1999) 283–293.
[3] T. Uchida, Y. Ohya, Application of a large-eddy simulation to wind system predictions over complex terrain, Proceedings of the 16th Japan Wind Engineering Symposium, 2000, pp. 59–64 (in Japanese).
[4] J. Smagorinsky, General circulation experiments with the primitive equations, Part 1, Basic experiments, Mon. Weather Rev. 91 (1963) 99–164.
[5] J. Kim, P. Moin, Application of a fractional-step method to incompressible Navier–Stokes equations, J. Comput. Phys. 59 (1985) 308–323.
[6] T. Kajishima, Upstream-shifted interpolation method for numerical simulation of incompressible flows, Bull. Jpn. Soc. Mech. Eng. B 60–578 (1994) 3319–3326 (in Japanese).
[7] T. Kawamura, H. Takami, K. Kuwahara, Computation of high Reynolds number flow around a circular cylinder with surface roughness, Fluid Dyn. Res. 1 (1986) 145–162.